Mechanism and Constitutive Model of a Continuum Robot for Head and Neck Cancer Radiotherapy.

Olalekan Ogunmolu[†], Xinmin Liu[⋆], Nicholas Gans[‡], and Rodney Wiersma[⋆]

***Abstract*—We present a parallel soft robot mechanism and its model for the correction of the complete degrees of freedom motion of a patient's deviation from target pose in head and neck cancer radiation therapy. Our design goal is to provide a real-time head and neck manipulation and motion correction that is needed during frameless and maskless cancer radiation therapy. Each soft robot within the mechanism contracts or expands in a radially symmetric fashion, under the isochoric property of its incompressible material body, around the patient's cranial region. We analyze the mechanical arrangement, derive the deformation model, and then present simulation results. Our results show consistency with the AAPM positioning accuracy guidelines, with less than $1mm$ displacement errors in the test deformation cases of the proposed model. In a follow-up work [1], we provide the kinematics and dynamics of the mechanism when the IAB mechanism interacts with the cranial region of the head.**

I. Introduction

Radiation therapy (RT) is an increasingly effective cancer treatment modality, with more than half of all cancer patients managed with RT having higher survival rates [2]. To assure optimal dose delivery, it is important for the patient to remain in a stable pose on the treatment machine during treatment. The current clinical convention is to immobilize the patient with rigid metallic frames and masks in a process called frame- and mask-based immobilization (see Figure 1). However, these immobilization mechanisms attenuate the radiation dose (lowering treatment quality), lack real-time motion compensation (hence the need for stopping the treatment when the patient deviates from a target position beyond a given threshold), and they cause patient discomfort and pain [3].

Systems such as the Cyberknife (see Figure 2), though ensuring complete non-invasive radiotherapy with implanted tiny gold fiducials to differentiate tumors from healthy tissues, are incapable of closed-loop, real-time head motion correction when the treatment beam is on. This is because they are only capable of compensating motion with pre-calculated trajectories. Furthermore, they have limited effectiveness given their non-compliant parts that assume rigidity of the patient's body.

Techniques devised for immobilization so far in clinics range from open-loop motion compensation systems (where the whole treatment is stopped whenever the patient deviates from target), to closed-loop robot-in-the-loop compensation systems. Initial F&M RT research consisted of semi-rigid and soft devices around the patient's head and neck (H&N) region without a closed-loop feedback controller. These techniques were mostly evaluative studies meant to investigate the feasibility of non-rigid immobilization techniques in treatment planning [4]–[9]. Closed-loop approaches achieve a higher real-time positioning accuracy, in a technique called frameless and maskless (F&M) RT. These closed-loop mechanisms utilize rigid parallel robots which provide better positioning accuracy owing to their inherent defenses against the large flexure torques and error magnification of open kinematic chains. With rigid electro-mechanical links connected at discrete joints, they correct motions in controlled settings. Example implementations include the steel-cast assembled 4-DOF robot of [10], the HexaPOD parallel manipulator of [11], or the fabricated Stewart-Gough platform of [12]. These rigid parallel robots that have emerged as a means of motion-correction come with the hazards that

- they share their dextrous workspace with the patients' body and tissues – a safety concern since these robots' rigid mechanical components exhibit almost no compliance,

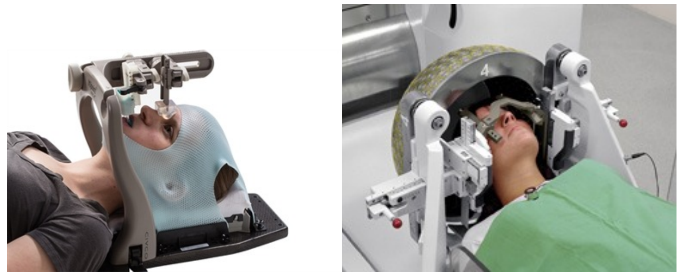

Fig. 1: Mask/Frame Immobilization in Frame-based RT. [Image best visualized in colored print].

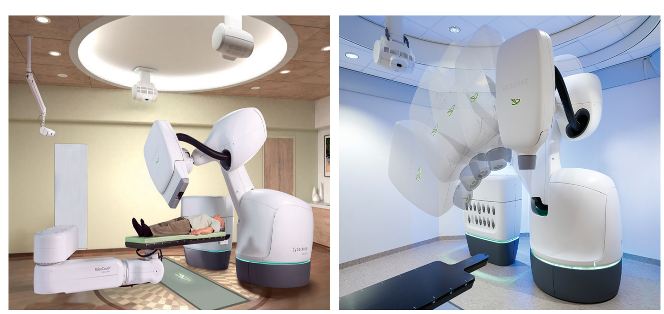

Fig. 2: The Cyberknife and 6-DOF robotic couch system. ©Accuray Inc. [Image best visualized in colored ink].

[†]Perelman School of Medicine, The University of Pennsylvania, Philadelphia, PA 19104, USA ogunmolo@pennmedine.upenn.edu

[⋆]Department of Radiation Oncology, The University of Chicago, Chicago, IL 60637, USA {xmliu, rwiersma}@uchicago.edu

[‡]Automation & Intelligent Systems Division, The University of Texas at Arlington, Arlington, TX, USA. nick.gans@uta.edu

The research reported in this publication was supported by National Cancer Institute of the National Institutes of Health under award number R01CA227124.

- their lack of structural compliance mean that the patient experiences the push"hard shocks" when the end effector moves,
- they are incapable of providing sophisticated motion compensation that may be needed for respiratory and internal organs displacement that often cause deviation from target.

In these implementations, the attenuation of the ionizing radiation owing to interference with the mechanical robot components is often left unresolved. It is noteworthy that recent developments such as [13] proposes moving the robot underneath the patient's body, away from the beam. However, it is not yet certain that this would fully resolve the radiation attenuation question. The human body is a natural system that needs to be manipulated with materials that absorb much of the energy arising out of collisions. To mitigate these issues, we proposed using inflatable air bladders (IABs) as motion compensators during F&M RT treatment [14]–[17]. Our IABs are continuum, compliant, and configurable (C3) soft robot (SoRo) actuators that provide therapeutic patient motion compensation during RT. These IABs inflate, deflate, expand or contract governed by their material moduli, internal pressurization and incompressibility constraints when given a reference trajectory. To our knowledge, ours are the first to explore C3 materials as actuation systems for cranial manipulation in robotic radiotherapy.

Here, we present a C3 parallel kinematic soft robot mechanism as well as analyze and test the constitutive model of our new class of IABs. The rest of this paper is structured as follows: in § II, we present the overall C3 kinematic mechanism; we analyze the deformation properties of the IAB in § III; we then provide and discuss simulation results in § IV. We conclude the paper in § V.

II. Mechanism Description

In previous works [14]–[16], we relied on a data-driven system identification approach to realize the overall system dynamics. Our resultant system model lumped the patient, treatment couch, as well as IAB models. These models lacked high-fidelity such that they necessitated the memory-based adaptive control composite laws that had to be derived from inverse Lyapunov analysis in works such as [16]. Furthermore, the approximation model of the ensuing neural-network component controller is a feature that required extensive training to realize a suitable controller for our H&N immobilization. Our goal here is to realize constitutive models for the IAB chains and peripheral actuation mechanisms – capable of manipulating the patient's H&N's complete DOF motion in real-time during RT. This would enable us write closed-form expressions for the IAB chains' complete kinematics.

A. Motion-Compensation Setup

We now describe the mechanism of the complete motion compensation system. We propose 3 IAB kinematic chains totaling 8 IABs around the patient's H&N region as illustrated in the abstraction diagram of Figure 3. The IABs are made out of silicone or rubber materials with a Poisson ration of approximately 0.5. They have two internal cavities. The internal cavity ensures the hollow IAB can hold the head in place before treatment. The outer shell encapsulates the internal shell such that local volume preservation is fulfilled between configuration changes. This isochoric property and the incompressibility constraints of the IAB material property is important in our mathematical derivations of the mechanism's constitutive model.

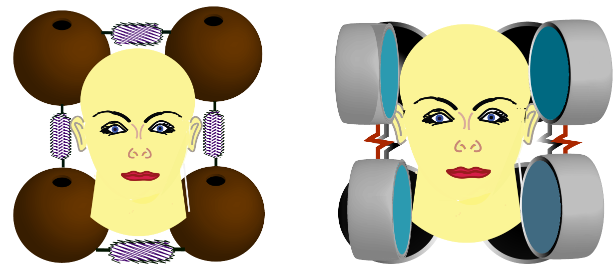

Fig. 3: An abstraction of the patient's position correction mechanism. In the left image, there are four IABs that constitute the base kinematic chain. They lift the head along the Z-axis (up or down on the treatment table) as well as provide pitch motion corrections. On the right, the side kinematic chains provide roll and yaw motion corrections. [Image best visualized in colored print].

There exists two IAB chains to each side of the patient's cranial region. These chains consist of two IABs, linked together by a passive extensible connector to accommodate head contact throughout manipulation – an important property as we shall see in the contact kinematics derivations [1]. Each IAB makes contact with the forehead and the chin/neck region at either symmetry of the patient's head. Underneath the patient's H&N regions is a closed kinematic chain. This chain consists of four IABs, each positioned at four cardinal contact points beneath the patient's H&N region (see Figure 3, and Figure 4). The IABs change their configuration based on air that is conveyed into or out of their internal cavities when the sensed deviation of the patient from a target exceeds a pose setpoint or desired trajectory path . The degrees of freedom of the mechanism of Figure 3 can be determined using *Gruëbler-Kutzbach's mobility condition*, wherein the number of degrees of freedom of the mechanism is given by (when the actuation results in a non-planar workspace configuration)

$$F = 6(N - g) + \sum_{i=1}^{g} f_i \tag{1}$$

where N is the number of links in the mechanism, g is the number of joints, f_i is the total number of degrees of freedom for the ith joint. where through equations (1), the mechanism of has 16 DOFs given its $N = 8$ links, $g = 8$ joints, and each joint is constrained along 2 DOFs .

B. Finite Elastic Deformation Model

We propose a finite elastic deformation model [19]–[21], based on the deformation invariants of the stored energy function of each IAB. In what follows, we briefly describe our motivation for devising a finite elastic deformation model. The

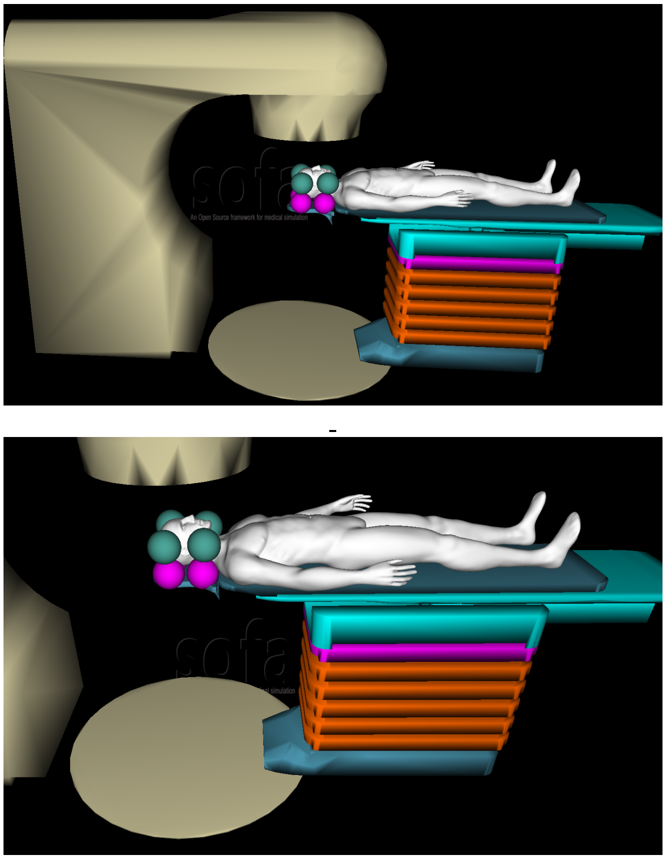

Fig. 4: System setup in the SOFA Framework Architecture. **Top**: Gantry, Turntable, Patient and IAB Chains around the patient's H&N Region. **Bottom**: Close-up view of compensating IABs around patient's H&N region with the patient lying in a supine position on the treatment couch. [Image best visualized in colored print].

constant curvature approach for parameterizing the deformation of continuum robots [22]–[24] has played significant role in the kinematic synthesis of deformable continuum models over the past three decades. Under this framework, the configuration space of a soft robot module is parameterized by the curvature of an arc projected on the soft robot's body, the arc's length, and the angle subtended by a tangent along that arc. The relationship between these parameters are typically found using differential kinematics with a Frenet-Serret frame that models a curve on the soft robot's surface with or without torsion. By abstracting an infinite dimensional structure to 3D, large portions of the manipulator dynamics are discarded under the assumption that the actuator design is symmetric and uniform in shape. This makes the constant curvature model overly simplified so that it often exhibits poor performance in position control [25]. While the Cosserat brothers' beam theory has been relatively successful in modeling soft continuum dynamics [26], [27], its complexity, and sensing cost does not justify the alternatives [28].

Contributions:

- We propose a motion correction mechanism that largely avoids dose attenuation, whilst providing patient comfort during motion correction in F&M cancer RT;

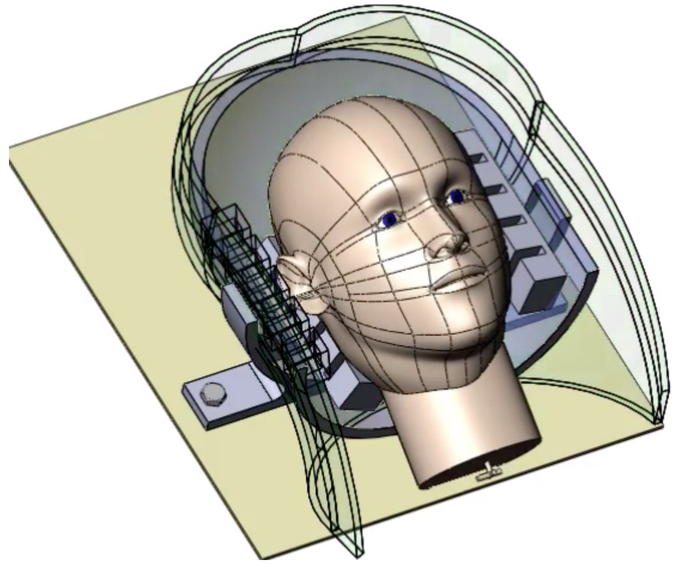

Fig. 5: Radio transparent wearable semi-plastic mask model that holds the IABs in place around the patient's H&N region. This follows our design in [18]. Unlike frame-based immobilization systems, the head can undergo complete motion manipulation inside the adjustable wearable mask. [Image best visualized in colored print.]

- For the proposed mechanism, we construct a constitutive model for its constituent C3 IABs by extending the principles of nonlinear elastic deformations [20], [21] to the isochoric strain deformations of these IAB semi-rigid bodies (which are constructed out of materials with incompressible walls);
- We then analyze their deformation under stress, strain, internal pressurization, and an arbitrary hydrostatic pressure.

This kinematic model will then be used to develop the kinematics and Lagrangian equations of the dynamics of the multi-dof motion correction mechanism. Particularly, we analyze the deformation of a single semi-rigid robot body. In a follow-up paper [1], we address the kinematics, dynamics and control of the overall actuation system.

III. Deformation Analysis of an IAB

In this section, we present the deformation analysis of the mechanism: we address the invariants of deformation, and strain deformation. We then analyze the stress laws and constitutive relations that govern the IAB deformation; we conclude the section by solving the boundary value problem under the assumptions of *isochoricity* and *incompressibility* of the IAB material skins. We present the kinematics of the IAB based on a relationship between internal pressure, Cauchy stress, stored strain energy, and the radii of the IAB. The IABs are made out of rubber components which have the distinct property of incompressibility with a Poisson ratio of approximately 0.5 [29]. Our overarching assumption is that volume does not change locally during deformation at a configuration $\chi(t)$ at time t. Since we consider only final configurations of the soft robot, we drop the explicit dependence of a configuration on

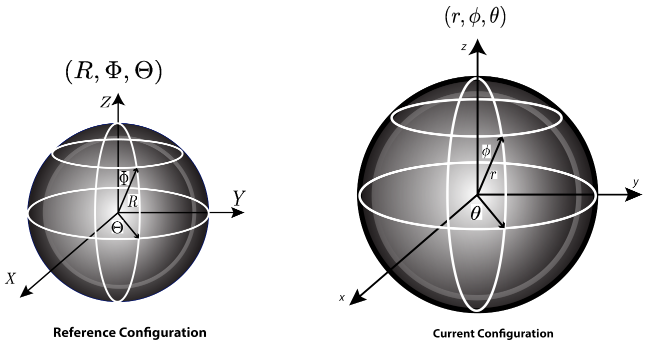

Fig. 6: Deformation in spherical polar coordinates.

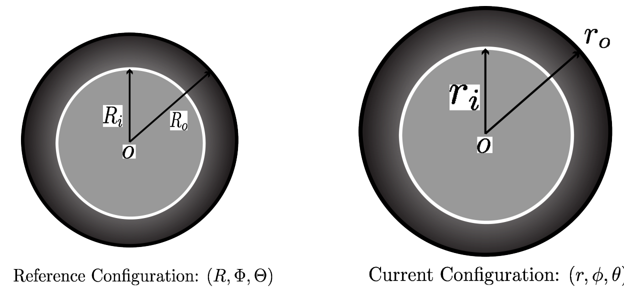

Fig. 7: Radii change under deformation.

time and write it as χ. We refer readers to background reading materials in [20], [30] and [29].

A. Deformation Invariants

For an elastic, and incompressible IAB under the action of applied forces, the deformation is governed by a stored energy function, W, which captures the physical properties of the material [31]. We choose two invariants namely, I_1, and I_2, described in terms of the principal extension ratios, $\lambda_r, \lambda_\phi, \lambda_\theta$, of the IAB's strain ellipsoids. They are defined as,

$$I_1 = \lambda_r^2 + \lambda_\phi^2 + \lambda_\theta^2, \quad \text{and} \quad I_2 = \lambda_r^{-2} + \lambda_\phi^{-2} + \lambda_\theta^{-2}. \tag{2}$$

Under the incompressibility assumptions of the IAB material, it follows that $\lambda_r \lambda_\phi \lambda_\theta = 1$ [21]. In spherical coordinates, the change in polar/azimuth angles as well as radii from the reference to current configurations are as illustrated in Figure 6. Forces that produce deformations are derived using the strain energy-invariants relationship, *i.e.* , $\frac{\partial W}{\partial I_1}$ and $\frac{\partial W}{\partial I_2}$.

B. Analysis of Strain Deformations

Suppose a particle on the IAB material surface in the reference configuration has coordinates (R, Φ, Θ) defined in spherical polar coordinates (see Figure 6), where R represents the radial distance of the particle from a fixed origin, Θ is the azimuth angle on a reference plane through the origin and orthogonal to the polar angle, Φ. Denote the internal and external radii as R_i, and R_o respectively. We define the following constraints,

$$R_i \le R \le R_o, \quad 0 \le \Theta \le 2\pi, \quad 0 \le \Phi \le \pi. \tag{3}$$

Now, suppose that the IAB undergoes deformation under the application of pressure on the internal IAB walls as depicted in Figure 7. Arbitrary points A and A' in the reference configuration become Q and Q' in the current configuration. Suppose that the vector that describes the *fiber* that connects points A and A' is $a = a_R \boldsymbol{e}_r + a_\Theta \boldsymbol{e}_\Theta + a_\Phi \boldsymbol{e}_\Phi$ where $\boldsymbol{e}_R, \boldsymbol{e}_\Theta$, and $\boldsymbol{e}_\Phi$ are respectively the basis vectors for polar directions R, Θ, and Φ such that its axial length stretches *uniformly* by an amount $\lambda_z = \frac{r}{R}$.We assume that there are internal constraints such that spherical symmetry is maintained during deformation of the incompressible IAB material shell so that we have the following constraints in the current configuration

$$r_i \le r \le r_o, \quad 0 \le \theta \le 2\pi, \quad 0 \le \phi \le \pi. \tag{4}$$

The radial vectors $\mathbf{R}$ and $\mathbf{r}$ are given in spherical coordinates as,

$$\mathbf{R} = \begin{bmatrix} R\cos\Theta\,\sin\Phi, \\ R\,\sin\Theta\,\sin\Phi, \\ R\cos\Phi \end{bmatrix} \quad \text{and} \quad \mathbf{r} = \begin{bmatrix} r\cos\theta\,\sin\phi, \\ r\,\sin\theta\,\sin\phi, \\ r\cos\phi \end{bmatrix}. \tag{5}$$

The material volume $\frac{4}{3}\pi\left(R^3 - R_i^3\right)$ contained between spherical shells of radii R and R_i remains constant throughout deformation, being equal in volume to $\frac{4}{3}\pi\left(r^3 - r_i^3\right)$ so that

$$\begin{aligned} \frac{4}{3}\pi\left(R^3 - R_i^3\right) &= \frac{4}{3}\pi\left(r^3 - r_i^3\right) \\ r^3 &= R^3 + r_i^3 - R_i^3. \end{aligned} \tag{6}$$

The homogeneous deformation between the two configurations imply that

$$r^3 = R^3 + r_i^3 - R_i^3, \quad \theta = \Theta, \quad \phi = \Phi, \tag{7}$$

where the coordinates obey the constraints of equations (3) and (4). We have the radial stretch as $\lambda_r = \frac{R^2}{r^2}$. Owing to the preservation of spherical symmetry, the *Lagrangean* and *Eulerian* axes coincide, with one axis aligned to the radial axis of the sphere and the other pair oriented arbitrarily normal to it so as to form a mutually orthogonal triad. The principal stretches along the azimuthal and zenith axes imply that $\lambda_\theta = \lambda_\phi$. Since for an isochoric deformation, $\lambda_r \cdot \lambda_\theta \cdot \lambda_\phi = 1$, the principal extension ratios are

$$\lambda_r = \frac{R^2}{r^2}; \lambda_\theta = \lambda_\phi = \frac{r}{R}.$$

The Mooney-Rivlin strain energy for small deformations as a function of the strain invariants of (2), is,

$$W' = C_1(I_1 - 3) + C_2(I_2 - 3), \tag{8}$$

where C_1 and C_2 are appropriate choices for the IAB material moduli. The Mooney form (8) has been shown to be valid even for large elastic deformations, provided that the elastic materials exhibit incompressibility and are isotropic in their reference configurations [19]. For mathematical scaling purposes that will soon become apparent, we rewrite (8) as $W = \frac{1}{2}W'$ so that

$$W = \frac{1}{2}C_1(I_1 - 3) + \frac{1}{2}C_2(I_2 - 3). \tag{9}$$

Note that equation (8) or (9) becomes the neo-Hookean strain energy relation when $C_2 = 0$. The deformation gradient $\mathbf{F}$ in

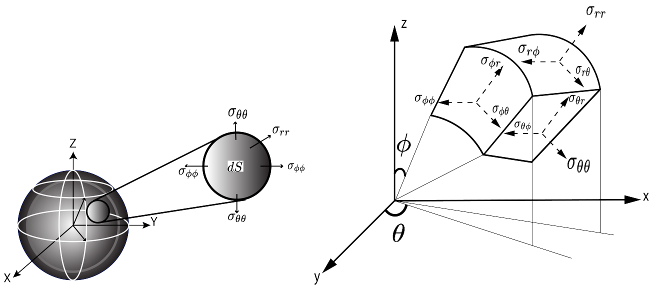

Fig. 8: Body stress distribution on the IAB's differential surface, dS.

spherical polar coordinates, becomes

$$\begin{aligned}\mathbf{F} &= \lambda_r \boldsymbol{e}_r \otimes \boldsymbol{e}_R + \lambda_\phi \boldsymbol{e}_\phi \otimes \boldsymbol{e}_\Phi + \lambda_\theta \boldsymbol{e}_\theta \otimes \boldsymbol{e}_\Theta \\ &= \frac{R^2}{r^2}\boldsymbol{e}_r \otimes \boldsymbol{e}_R + \frac{r}{R}\boldsymbol{e}_\phi \otimes \boldsymbol{e}_\Phi + \frac{r}{R}\boldsymbol{e}_\theta \otimes \boldsymbol{e}_\Theta, \end{aligned} \tag{10}$$

where $\otimes$ denotes the dyadic product [20]. The invariant equations, in polar coordinates, are therefore a function of the right Cauchy-Green and finger deformation tensors *i.e.* ,

$$I_1 = \mathbf{tr}(\mathbf{C}) = \frac{R^4}{r^4} + \frac{2\,r^2}{R^2},\ I_2 = \mathbf{tr}\left(\mathbf{C}^{-1}\right) = \frac{r^4}{R^4} + \frac{2\,R^2}{r^2}, \tag{11}$$

where, $\mathbf{C} = \mathbf{F}^T\mathbf{F}$ and $\mathbf{B} = \mathbf{F}\mathbf{F}^T$ are the right and left Cauchy-Green tensors.

C. Stress Laws and Constitutive Equations

We are concerned with the magnitudes of the differential stress on the IAB skin from a mechanical point of view. Since the IAB deforms at ambient temperature, we assume that thermodynamic properties such as temperature and entropy have negligible contribution. The IAB material stress response, $\mathbf{G}$, at any point on the IAB's boundary at time t determines the Cauchy stress, $\boldsymbol{\sigma}$, as well as the history of the motion up to and at the time t. The constitutive relation for the nominal stress deformation for an elastic IAB material is given by

$$\boldsymbol{\sigma} = \mathbf{G}(\mathbf{F}) + q\mathbf{F}\frac{\partial \boldsymbol{\Lambda}}{\partial \mathbf{F}}(\mathbf{F}), \tag{12}$$

where $\mathbf{G}$ is a functional with respect to the configuration $\boldsymbol{\chi}_t$, q acts as a Lagrange multiplier, and $\boldsymbol{\Lambda}$ denotes the internal (incompressibility) constraints of the IAB system. For an incompressible material, the indeterminate Lagrange multiplier becomes the hydrostatic pressure *i.e.* $q = -p$ [30]. The incompressibility of the IAB material properties imply that $\boldsymbol{\Lambda} \equiv \det \mathbf{F} - 1$. As such, we have from the special case of Jacobi's formula for the derivative of a matrix determinant that (12) becomes

$$\begin{aligned}\boldsymbol{\sigma} &= \mathbf{G}(\mathbf{F}) - p\mathbf{F}\text{adj}^{\,T}(\mathbf{F}) \\ &= \mathbf{G}(\mathbf{F}) - p\mathbf{F}\mathbf{F}^{-T}\det(\mathbf{F}) \\ &= \mathbf{G}(\mathbf{F}) - p\mathbf{I} \end{aligned} \tag{13}$$

In terms of the stored strain energy, we can rewrite (13) as

$$\boldsymbol{\sigma} = \begin{bmatrix} \sigma_{rr} & \sigma_{r\phi} & \sigma_{r\theta} \\ \sigma_{\phi r} & \sigma_{\phi\phi} & \sigma_{\phi\theta} \\ \sigma_{\theta r} & \sigma_{\theta\phi} & \sigma_{\theta\theta} \end{bmatrix} = \frac{\partial W}{\partial \mathbf{F}}\mathbf{F}^T - p\mathbf{I}, \tag{14}$$

where $\mathbf{I}$ is the identity tensor and p represents an arbitrary hydrostatic pressure. A visualization of the component stresses of (14) on the walls of the IAB material is illustrated in Figure 8. It follows that the constitutive law that governs the Cauchy stress tensor is

$$\begin{aligned}\boldsymbol{\sigma} &= \frac{\partial W}{\partial \mathrm{I}_1}\cdot\frac{\partial \mathrm{I}_1}{\partial \mathbf{F}}\mathbf{F}^T + \frac{\partial W}{\partial \mathrm{I}_2}\cdot\frac{\partial \mathrm{I}_2}{\partial \mathbf{F}}\mathbf{F}^T - p\mathbf{I} \\ &= \frac{1}{2}C_1\frac{\partial \mathbf{tr}\left(\mathbf{F}\mathbf{F}^T\right)}{\partial \mathbf{F}}\mathbf{F}^T + \frac{1}{2}C_2\frac{\partial \mathbf{tr}(\left[\mathbf{F}^T\mathbf{F}\right]^{-1})}{\partial \mathbf{F}}\mathbf{F}^T - p\,\mathbf{I} \\ &= \frac{1}{2}C_1\left(2.\mathbf{F}\mathbf{F}^T\right) + \frac{1}{2}C_2\left(-2\mathbf{F}(\mathbf{F}^T\mathbf{F})^{-2}\right)\mathbf{F}^T - p\,\mathbf{I} \\ &= C_1\mathbf{F}\mathbf{F}^T - C_2\left(\mathbf{F}^T\mathbf{F}\right)^{-1} - p\mathbf{I} \\ \boldsymbol{\sigma} &= C_1\mathbf{B} - C_2\mathbf{C}^{-1} - p\mathbf{I}. \end{aligned} \tag{15}$$

It follows that the normal stress components are

$$\sigma_{rr} = -p + C_1\frac{R^4}{r^4} - C_2\frac{r^4}{R^4} \tag{16a}$$

$$\sigma_{\theta\theta} = \sigma_{\phi\phi} = -p + C_1\frac{r^2}{R^2} - C_2\frac{R^2}{r^2}. \tag{16b}$$

D. IAB Boundary Value Problem

Here, we analyze the stress and internal pressure of the IAB at equilibrium. Consider the IAB with boundary conditions given by,

$$\sigma_{rr}|_{R=R_o} = -P_{\text{atm}}, \quad \sigma_{rr}|_{R=R_i} = -P_{\text{atm}} - P \tag{17}$$

where P_{atm} is the atmospheric pressure and $P > 0$ is the internal pressure exerted on the walls of the IAB above P_{atm} *i.e.* , $P > P_{\text{atm}}$. Suppose that the IAB stress components satisfy hydrostatic equilibrium, the equilibrium equations for the body force $\boldsymbol{b}'s$ physical component vectors, b_r, b_θ, b_ϕ are

$$\begin{aligned}-b_r = &\frac{1}{r^2}\frac{\partial r^2\sigma_{rr}}{\partial r} + \frac{1}{r\sin\phi}\frac{\partial \sin\phi\sigma_{r\phi}}{\partial \phi} + \frac{1}{r\sin\phi}\frac{\partial \sigma_{r\theta}}{\partial \theta} \\ &- \frac{1}{r}(\sigma_{\theta\theta} + \sigma_{\phi\phi}) \end{aligned} \tag{18a}$$

$$\begin{aligned}-b_\phi = &\frac{1}{r^3}\frac{\partial r^3\sigma_{r\phi}}{\partial r} + \frac{1}{r\sin\phi}\frac{\partial \sin\phi\sigma_{\phi\phi}}{\partial \phi} + \frac{1}{r\sin\phi}\frac{\partial \sigma_{\theta\phi}}{\partial \theta} \\ &- \frac{\cot\phi}{r}(\sigma_{\theta\theta}) \end{aligned} \tag{18b}$$

$$-b_\theta = \frac{1}{r^3}\frac{\partial r^3\sigma_{\theta r}}{\partial r} + \frac{1}{r\sin^2\phi}\frac{\partial \sin^2\phi\sigma_{\theta\phi}}{\partial \phi} + \frac{1}{r\sin\phi}\frac{\partial \sigma_{\theta\theta}}{\partial \theta} \tag{18c}$$

(see [32]). From the equation of balance of linear momentum (*Cauchy's first law of motion*), we have that

$$\text{div}\ \boldsymbol{\sigma}^T + \rho\mathbf{b} = \rho\dot{\mathbf{v}} \tag{19}$$

where ρ is the IAB body mass density, div is the divergence operator, and $\mathbf{v}(\mathbf{x}, t) = \dot{\boldsymbol{\chi}}_t(\boldsymbol{X})$ is the velocity gradient. Owing to the incompressibility assumption, we remark in passing that the mass density is uniform throughout the body of the IAB material. When the IAB is at rest, $\dot{\mathbf{v}}_t(\mathbf{x}) = 0\,\forall\,\mathbf{x} \in \mathcal{B}$ such that equation (19) loses its dependence on time. The assumed regularity of the IAB in the reference configuration thus leads to the steady state conditions for Cauchy's first equation; the stress field $\boldsymbol{\sigma}$ becomes *self-equilibrated* by virtue of the spatial divergence and the symmetric properties of the stress tensor, so that we have

$$\textbf{div}\ \boldsymbol{\sigma} = 0, \tag{20}$$

Equation 20 is satisfied if the hydrostatic pressure p in (15) is independent of θ and ϕ. Therefore, we are left with (18a) so that we have

$$\frac{1}{r}\frac{\partial}{\partial r}(r^2\sigma_{rr}) = (\sigma_{\theta\theta} + \sigma_{\phi\phi}). \tag{21}$$

Expanding, we find that

$$\begin{aligned}\frac{1}{r}\left[r^2\frac{\partial \sigma_{rr}}{\partial r} + \sigma_{rr}\frac{\partial(r^2)}{\partial r}\right] &= (\sigma_{\theta\theta} + \sigma_{\phi\phi}) \\ r\frac{\partial \sigma_{rr}}{\partial r} &= \sigma_{\theta\theta} + \sigma_{\phi\phi} - 2\sigma_{rr} \qquad (22)\\ \frac{\partial \sigma_{rr}}{\partial r} &= \frac{1}{r}(\sigma_{\theta\theta} + \sigma_{\phi\phi} - 2\sigma_{rr}). \qquad (23)\end{aligned}$$

Integrating the above equation in the variable r, and taking $\sigma_{rr}(r_\circ) = 0$, we find that

$$\begin{aligned}\sigma_{rr}(\delta) &= -\int_\delta^{r_\circ} \frac{1}{r}(\sigma_{\theta\theta} + \sigma_{\phi\phi} - 2\sigma_{rr})dr, \ r_i \le \delta \le r_\circ \\ &= -\int_{r_i}^{r_\circ}\left[2C_1\left(\frac{r}{R^2} - \frac{R^4}{r^5}\right) + 2C_2\left(\frac{r^3}{R^4} - \frac{R^2}{r^3}\right)\right] dr.\end{aligned} \tag{24}$$

The above relation gives the radial stress in the current configuration. Suppose we are in the current configuration and we desire to revert to the reference configuration, we may carry out a change of variables from r to R as follows,

$$\begin{aligned}\sigma_{rr}(\Delta) &= -\int_\Delta^{R_\circ} \frac{1}{r}(\sigma_{\theta\theta} + \sigma_{\phi\phi} - 2\sigma_{rr})\frac{dr}{dR}dR, \ R_i \le \Delta \le R_\circ \\ &= -\int_\Delta^{R_\circ}\left[2C_1\left(\frac{1}{r} - \frac{R^6}{r^7}\right) - 2C_2\left(\frac{R^4}{r^5} - \frac{r}{R^2}\right)\right] dR.\end{aligned} \tag{25}$$

In the same vein, using the boundary condition of $(17)|_2$ and taking the ambient pressure $P_{\text{atm}} = 0$, we find that the internal pressure $P = -\sigma_{rr}(\delta) = -\sigma_{rr}(\Delta)$ *i.e.*

$$P(\delta) = \int_\delta^{r_\circ}\left[2C_1\left(\frac{r}{R^2} - \frac{R^4}{r^5}\right) + 2C_2\left(\frac{r^3}{R^4} - \frac{R^2}{r^3}\right)\right] dr \tag{26}$$

$$P(\Delta) \equiv \int_\Delta^{R_\circ}\left[2C_1\left(\frac{1}{r} - \frac{R^6}{r^7}\right) - 2C_2\left(\frac{R^4}{r^5} - \frac{r}{R^2}\right)\right] dR. \tag{27}$$

Equations (25) and (27) completely determine the deformation kinematics of the IAB material. Under the incompressibility of the IAB material properties we have,

$$r^3 = R^3 + r_i^3 - R_i^3, \text{ and } {r_\circ}^3 = R_\circ^3 + r_i^3 - R_i^3. \tag{28}$$

In [1], we relate the head and neck force to the contact forces on the IAB surface boundary using the component stress laws.

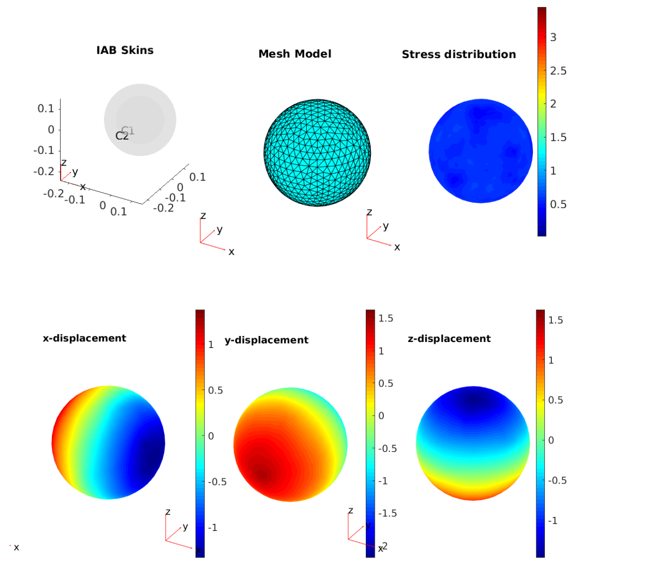

C_1	C_2	R_i	r_i	$R_\circ$	$r_\circ$	P	ν
1.1e4	2.2e4	10	13	15	16.60	14.552	0.45

Fig. 9: IAB Expansion I (Charts best visualized in colored print).

IV. Simulation

For a Cauchy-Elastic IAB material, we find the internal pressure needed for a desired deformation using (27). The results shown in Figures 9, 10, 11 and 12 respectively highlight the deformation response of the IAB material measured in terms of displacements along the x, y, and z directions. We conduct simulations under expansion and compression with different realistic material properties (their properties are stated in the tables beneath the figures). Note that all IAB radii dimensions are in cm, the pressure is given in psi, C_1 and C_2 denote the IAB material moduli, and ν is the Poisson ratio of the body in the tables. We fix both materials' radii in the reference configuration and choose physically realistic volumetric moduli for the IAB materials. Notice that the outer IAB material in all the examples have a sturdier structure owing to the higher volumetric modulus to account for the semi-rigidity of the IAB material body and we expect that they will not be dented when in contact with the patient's head. This design is deliberate as it simplifies the IAB kinematics when during contact while preserving the continuum properties just derived.

A. Results: Volumetric Expansion

For the given cases, the calculated pressure, and associated physical properties of the IAB are as given in the tables beneath the figure. To simulate the IAB body deformation, we applied triangular meshes to the rigid IABs with finite element modeling. We then compute the pressure that is required to uniformly expand the IAB from a reference to a current configuration (given by the values of R_o and r_o in the tables). The computed mesh model is shown in the top middle of the charts while the stress distribution after the application of the

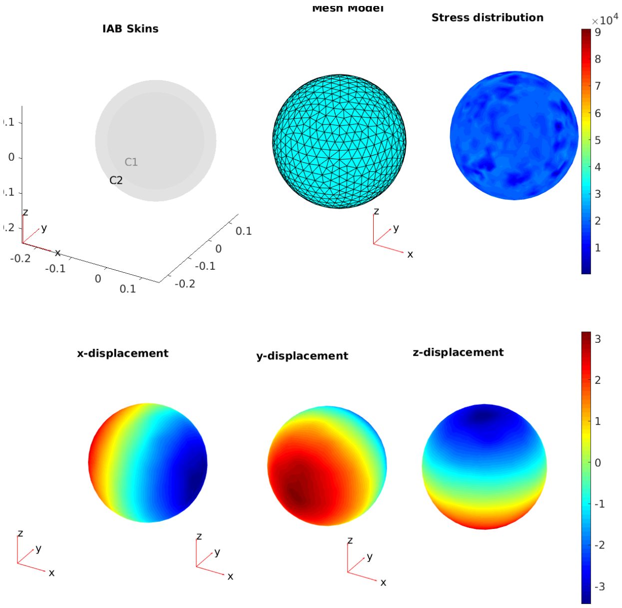

C_1	C_2	R_i	r_i	$R_\circ$	$r_\circ$	P	ν
$5e5$	$1e6$	7.5	12	10	13.21	14.5193	0.4995

Fig. 10: IAB Expansion II (Charts best visualized in colored print).

calculated pressure is shown in the upper-right corner of the figures. We chose a Poisson ratio of $0.45 - 0.5$ to model the incompressibility material properties of the IABs.

In the compression case of Figure 9, our goal was to uniformly expand the IAB from an outer radius of 15cm to 16.60cm in the current configuration. Notice a uniform expansion of 1.6cm along the three Cartesian axes of the IAB in the lower charts of Figure 9 as a consequence of (27). We notice a similar consistency in Figure 10 with a required expansion of 3.21cm. The IAB extends to $\sim 3.18cm$ along all three axes – exhibiting a positioning error of $0.3mm$.

B. Results: Volumetric Compression

In the deformation cases of Figures 11 and 12, we present a uniform contraction of representative volumes of the isotropic and incompressible IAB under the application of the derived internal pressure for a desired radial shrink. The calculated negative pressures shown in the tables signify that air is being drawn out of the bladders. Again, we notice an almost uniform stress distribution on the IAB's body and an equal shrinking along the Cartesian axes of the IAB. For a required shrink of 1.17cm from the reference configuration of Figure 11, we notice a corresponding shrinkage along the desired directions by the required amount in the lower charts of the figure. For both figures of Figure 11 and Figure 12, notice that the deformation precision is well below the 2mm clinical accuracy recommended by the AAPM task group guidelines [33].

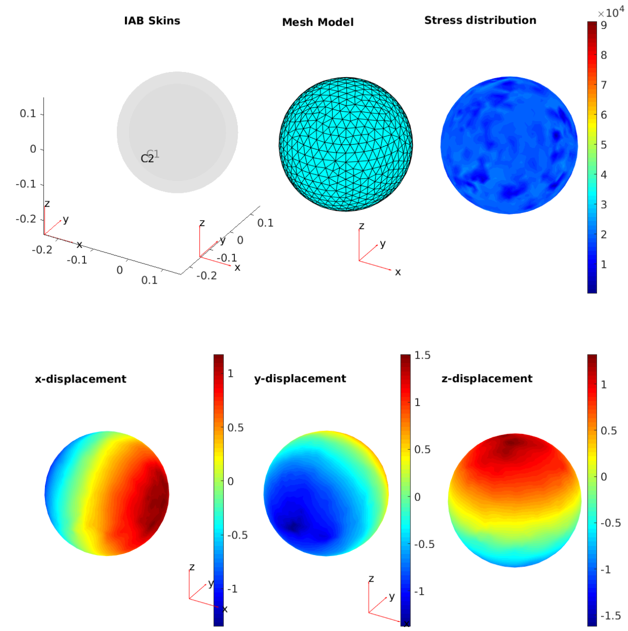

C_1	C_2	R_i	r_i	$R_\circ$	$r_\circ$	P	ν
$5e5$	$1.2e6$	12	10	15	13.83	-27.4	0.45

Fig. 11: IAB Compression I (Charts best visualized in colored print).

V. Conclusion

We have presented the motion-correction mechanism of a proposed IAB system during RT as well as the constitu-

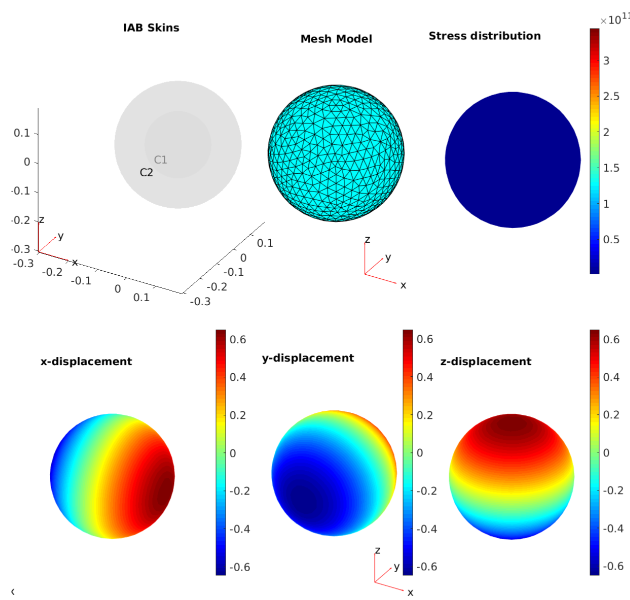

C_1	C_2	R_i	r_i	$R_\circ$	$r_\circ$	P	ν
$1.1e12$	$2.2e10$	10	8	19	18.54	-27.4	0.495

Fig. 12: IAB Compression II (Charts best visualized in colored print).

tive model for the constituent C3 IABs. We analyzed the deformation of these IABs with finite elastic deformation theory. The deformation results presented in this work are well within the positioning accuracy requirements for H&N motion compensation requirements in cancer RT as defined in the guidelines of the American Association for Physicists in Medicine Task Group 42 [33]. The reader might ask, what happens when the head lies on the IAB, will the stress-strain constitutive relations hold given the natural tendency of the weight of the head to deform the IAB material? The key design to avoiding using spherical harmonics to characterize such possible cases is to properly choose the elasticity modulus of the outer IAB material skin such that in its equilibrium state, or during transitions between configurations, the IAB material holds the bulk compression/expansion property.

In a follow-up paper [1], we analyze the contact and deformation behavior of the IABs when they come in contact with the cranial region of the head. We then proceed to construct the kinematic model for the full head and neck positioning control in real-time frameless and maskless radiation therapy. Future work would include physical IAB and IAB chains build as well as the implementation of the model described in this work on test patient cases.

References

[1] O. Ogunmolu, E. Pearson, X. Liu, and R. Wiersma, "Kinematics and Dynamics of a Continuum Robot Immobilization Mechanism for Cancer Radiotherapy." 1, 2, 3, 6, 8

[2] L. Gaspar *et al.*, "Recursive Partitioning Analysis (rpa) of Prognostic Factors in three Radiation Therapy Oncology Group (rtog) Brain Metastases Trials," *Int. J. Radiat. Oncol. Biol. Phys.*, vol. 37, p. 745751, 1997. 1

[3] T. Takakura, T. Mizowaki, M. Nakata, S. Yano, T. Fujimoto, Y. Miyabe, M. Nakamura, and M. Hiraoka, "The geometric accuracy of frameless stereotactic radiosurgery using a 6d robotic couch system," *Physics in Medicine & Biology*, vol. 55, no. 1, p. 1, 2009. 1

[4] L. I. Cerviño, N. Detorie, M. Taylor, J. D. Lawson, T. Harry, K. T. Murphy, A. J. Mundt, S. B. Jiang, and T. A. Pawlicki, "Initial Clinical Experience with a Frameless and Maskless Stereotactic Radiosurgery Treatment," *Practical Radiation Oncology*, vol. 2, no. 1, pp. 54–62, 2012. 1

[5] L. I. Cerviño, T. Pawlicki, J. D. Lawson, and S. B. Jiang, "Frame-less and mask-less cranial stereotactic radiosurgery: a feasibility study," *Physics in medicine and biology*, vol. 55, no. 7, p. 1863, 2010. 1

[6] M. J. Murphy, R. Eidens, E. Vertatschitsch, and J. N. Wright, "The effect of transponder motion on the accuracy of the calypso electromagnetic localization system," *International Journal of Radiation Oncology* Biology* Physics*, vol. 72, no. 1, pp. 295–299, 2008. 1

[7] A. Navarro-Martin, J. Cacicedo, O. Leaman, I. Sancho, E. García, V. Navarro, and F. Guedea, "Comparative analysis of thermoplastic masks versus vacuum cushions in stereotactic body radiotherapy," *Radiation Oncology*, vol. 10, no. 1, p. 176, 2015. 1

[8] G. Li, A. Ballangrud, M. Chan, R. Ma, K. Beal, Y. Yamada, T. Chan, J. Lee, P. Parhar, J. Mechalakos, *et al.*, "Clinical Experience with two Frameless Stereotactic Radiosurgery (fsrs) Systems using Optical Surface Imaging for Motion Monitoring," *Journal of Applied Clinical Medical Physics/American College of Medical Physics*, vol. 16, no. 4, p. 5416, 2015. 1

[9] A. Krauss, S. Nill, M. Tacke, and U. Oelfke, "Electromagnetic real-time tumor position monitoring and dynamic multileaf collimator tracking using a siemens 160 mlc: Geometric and dosimetric accuracy of an integrated system," *International Journal of Radiation Oncology* Biology* Physics*, vol. 79, no. 2, pp. 579–587, 2011. 1

[10] X. Liu, A. H. Belcher, Z. Grelewicz, and R. D. Wiersma, "Robotic stage for head motion correction in stereotactic radiosurgery," in *2015 American Control Conference (ACC)*. IEEE, 2015, pp. 5776–5781. 1

[11] C. Herrmann, L. Ma, and K. Schilling, "Model Predictive Control For Tumor Motion Compensation In Robot Assisted Radiotherapy," *IFAC Proceedings Volumes*, vol. 44, no. 1, pp. 5968–5973, 2011. 1

[12] A. Belcher, "Patient Motion Management with 6-DOF Robotics for Frameless and Maskless Stereotactic Radiosurgery," Ph.D. dissertation, The University of Chicago, 2017. 1

[13] X. Liu and R. D. Wiersma, "Optimization based trajectory planning for real-time 6DoF robotic patient motion compensation systems," *PloS one*, vol. 14, no. 1, p. e0210385, 2019. 2

[14] O. P. Ogunmolu, X. Gu, S. Jiang, and N. R. Gans, "A real-time, soft robotic patient positioning system for maskless head-and-neck cancer radiotherapy: An initial investigation," in *Automation Science and Engineering (CASE), 2015 IEEE International Conference on, Gothenburg, Sweden*. IEEE, 2015, pp. 1539–1545. 2

[15] O. P. Ogunmolu, X. Gu, S. Jiang, and N. R. Gans, "Vision-based control of a soft robot for maskless head and neck cancer radiotherapy," in *Automation Science and Engineering (CASE), 2016 IEEE International Conference on, Fort Worth, Texas*. IEEE, 2016, pp. 180–187. 2

[16] O. Ogunmolu, A. Kulkarni, Y. Tadesse, X. Gu, S. Jiang, and N. Gans, "Soft-neuroadapt: A 3-dof neuro-adaptive patient pose correction system for frameless and maskless cancer radiotherapy," in *IEEE/RSJ International Conference on Intelligent Robots and Systems (IROS), Vancouver, BC, CA*. IEEE, 2017, pp. 3661–3668. 2

[17] O. P. Ogunmolu, "A Multi-DOF Soft Robot Mechanism for Patient Motion Correction and Beam Orientation Selection in Cancer Radiation Therapy." Ph.D. dissertation, The University of Texas at Dallas; The University of Texas Southwestern Medical Center, 2019. 2

[18] Y. Almubarak, A. Joshi, O. Ogunmolu, X. Gu, S. Jiang, N. Gans, and Y. Tadesse, "Design and development of soft robot for head and neck cancer radiotherapy," in *Electroactive Polymer Actuators and Devices (EAPAD) XX*, vol. 10594. International Society for Optics and Photonics, 2018, p. 1059418. 3

[19] M. Mooney, "A theory of large elastic deformation," *Journal of applied physics*, vol. 11, no. 9, pp. 582–592, 1940. 2, 4

[20] R. Ogden, *Non-linear Elastic Deformations*. Mineola, New York: Dover Publicationbs, Inc., 1997. 2, 3, 4, 5

[21] L. R. G. Treloar, *The physics of rubber elasticity*. Oxford University Press, USA, 1975. 2, 3, 4

[22] M. W. Hannan and I. D. Walker, "Kinematics and the Implementation of an Elephant's Trunk Manipulator and Other Continuum Style Robots," *Journal of Robotic Systems*, vol. 20, no. 2, pp. 45–63, 2003. 3

[23] M. W. Hannan and I. D. Walker, "Novel Kinematics for Continuum Robots." Advances in Robot Kinematics, 2000, pp. 227–238. 3

[24] B. A. Jones and I. D. Walker, "Kinematics for Multisection Continuum Robots.pdf," vol. 22, no. 1, pp. 43–55, 2006. 3

[25] A. D. Kapadia, K. E. Fry, and I. D. Walker, "Empirical investigation of closed-loop control of extensible continuum manipulators," in *2014 IEEE/RSJ International Conference on Intelligent Robots and Systems*. IEEE, 2014, pp. 329–335. 3

[26] F. Renda, M. Giorelli, M. Calisti, M. Cianchetti, and C. Laschi, "Dynamic model of a multibending soft robot arm driven by cables," *IEEE Transactions on Robotics*, vol. 30, no. 5, pp. 1109–1122, 2014. 3

[27] D. Trivedi, A. Lotfi, and C. D. Rahn, "Geometrically Exact Models For Soft Robotic Manipulators," *IEEE Transactions on Robotics*, vol. 24, no. 4, pp. 773–780, 2008. 3

[28] T. George Thuruthel, Y. Ansari, E. Falotico, and C. Laschi, "Control Strategies for Soft Robotic Manipulators: A Survey," *Soft Robotics*, vol. 5, no. 2, pp. 149–163, 2018. 3

[29] A. Gent, *Engineering with Rubber. How to Design Rubber Components*. Munich: Carl Hanser Verlag Publicationbs, 2012. 3, 4

[30] G. A. Holzapfel, T. C. Gasser, and R. W. Ogden, "A new constitutive framework for arterial wall mechanics and a comparative study of material models," *Journal of elasticity and the physical science of solids*, vol. 61, no. 1-3, pp. 1–48, 2000. 4, 5

[31] R. S. Rivlin and D. W. Saunders, "Large Elastic Deformations of Isotropic Materials. VII. Experiments on the Deformation of Rubber," *Philosophical Transactions of the Royal Society A: Mathematical, Physical and Engineering Sciences*, vol. 243, no. 865, pp. 251–288, 1950. 4

[32] Y.-c. Fung, P. Tong, and X. Chen, *Classical and computational solid mechanics*. World Scientific Publishing Company, 2001, vol. 2. 5

[33] T. H. Wagner, T. Yi, S. L. Meeks, F. J. Bova, B. L. Brechner, Y. Chen, J. M. Buatti, W. A. Friedman, K. D. Foote, and L. G. Bouchet, "A geometrically based method for automated radiosurgery planning," *International Journal of Radiation Oncology* Biology* Physics*, vol. 48, no. 5, pp. 1599–1611, 2000. 7, 8